Biointerface Research in Applied Chemistry
Open-Access Journal (ISSN: 2069-5837)

Article
Volume 13, Issue 6, 2023, 542
https://doi.org/10.33263/BRIAC136.542

Delivery of some Trapped Metal Elements in the Boron Nitride Nanocone: Application of Bio-Sensors in Cell Membrane using a DFT Evaluation

Fatemeh Mollaamin [1,*], Karim Zare [2], Sara Shahriari [3]

[1] Department of Biomedical Engineering, Faculty of Engineering and Architecture, Kastamonu University, Kastamonu, Turkey
[2] Department of Chemistry, Science and Research Branch, Islamic Azad University, Tehran, Iran
[3] Department of Chemistry, Central Tehran Branch, Islamic Azad University, Tehran, Iran
* Correspondence: smollaamin@gmail.com (F.M.);

Scopus Author ID 35848813100
Received: 29.10.2022; Accepted: 5.01.2023; Published: 7.02.2023

Abstract: Positive stranded In this article, it has been investigated the density functional theory (DFT) study on single metal atoms of Li, Na, K, Be, Mg, and Ca trapped in B_9N_9 and $B_{40}N_{40}$ nanocones as biosensors in our body. Boron nitride (BN) is one of the structures similar to different crystals of carbon. Those B–N bonds will be replaced in these structures instead of C–C bonds in carbon nanotubes. In this investigation, it has been accomplished the B3LYP// EPRII, EPRIII/ 6-311+G(d,p)/ lanl2dz to estimate the susceptibility of B_9N_9 and $B_{40}N_{40}$ nanocones for trapping metal atoms of Li, Na, K, Be, Mg, Ca through charge transfer, NQR, NMR, spectroscopy and HOMO-LUMO molecular orbital analysis. Finally, the obtained results have approved that $B_{40}LiN_{40}$, $B_{40}NaN_{40}$, $B_{40}KN_{40}$, $B_{40}BeN_{40}$, $B_{40}MgN_{40}$, and $B_{40}CaN_{40}$ with good resistance and the electrical conductivity can be applied as biosensors in transferring and releasing the metal atoms in the human body. These results could be generalized to other B_nN_n nanocones and may help their rational design for biosensors that conduct the reactions in the biocells.

Keywords: BN nanocone; biosensor; B_9N_9; $B_{40}N_{40}$; Li; Na; K; Be; Mg; Ca; DFT.

1. Introduction

Semiconductor nanostructures like fullerenes, nanotubes, and nanocones can be provided by trapping the metal atoms, which attract attention in various applications depending on the size, geometry, and strength [1-10].

In this research, a novel design has been proposed, the metal-semiconductor nanocones formed with the main group metals of the periodic table, including Li, Na, K, Be, Mg, and Ca. Carbon nanotubes' unique physicochemical and mechanical properties through their interaction with metals have made these structures a special potential for application. The metal-nanotube interactions in most experimental and theoretical investigations have been accomplished for carbon nanotubes with transition metal components such as a single atom or a metal cluster [11-15].

Other nanomaterial cases are boron nitride (BN) nanotubes, nanocages, or nanocones, which can be synthesized after exploring carbon nanotubes with high thermal stability, chemical inertness, and hardness [16-24].

During this time, it has been done some experimental and theoretical studies to fill BN nanotubes with 3*d* transition metals like Fe–Ni, Co, Mo, Ni, and $NiSi_2$, which have shown half-metallic behavior in some of these complexes [25-32].

Boron nitride nanotube (BNNT) usually exhibits semi-leading behavior, which is considered a proper alternative to carbon nanotubes. The properties of boron and nitrogen atoms which are the first neighbors of carbon in the periodic table, make BNNT an interesting subject of numerous studies [33-35].

The stable one-dimensional structure of BNNT was either theoretically recognized or experimentally synthesized [36]. Earlier studies have indicated that the ends of BNNTs are significant in the determination of their growth and also application properties [37]. BNNTs are composite nanotubes that have been synthesized successfully following the synthesis of carbon nanotubes (CNTs), but the electronic properties of BNNTs are different from that of CNTs [38-41].

BNNT is produced by rolling a single layer of sp^2 boron into a seamless hollow cylindrical tube with nanoscale dimensions. Moreover, nanotubes, their unique physical properties, exhibit various electrical properties. The geometrical and electronic structure of BNNTs can be described by a chiral vector, the angle between the axis of its hexagonal pattern and the axis of the tube which is presented by the (n_1; n_2) chirality's indices. When the indices are (n_1, 0) called zigzag, (n_1, n_1) called armchair, and (n_1, n_2) where $n_1 \neq 0$ and $n_2 \neq 0$ known as chiral BNNTs.

Although scientific efforts focused on the electrostatics properties and commercial applications of these materials, there have been no experimental structural data sufficiently accurate for the identification of the chirality's indices of BNNTs, especially for the kind of smaller diameter nanotubes. In this paper, we study the structural properties of BN rings obtained by bending a BN graphitic sheet. We, therefore, here only briefly review the symmetry treatment for hexagonal wrappings of tubes. BN nanostructures are polar through the ground charge on B and N atoms, producing a graphite form by alternating these two atoms [42]. Therefore, these structures are similar to carbon nanotubes with various physical properties and electrostatic interactions, which play an important role in distinguishing their elastic properties. However, the mechanical properties of both BNNTs and CNTs are approximately identical, like metals or semiconductors [43-49].

BNNT is produced by rolling a single layer of sp^2 boron into a seamless hollow cylindrical tube with nanoscale dimensions. The geometrical and electronic structure of BNNTs can be described by a chiral vector, the angle between the axis of its hexagonal pattern and the axis of the tube presented by the (n_1; n_2) chirality's indices. When the indices are (n_1, 0) called zigzag, (n_1, n_1) called armchair, and (n_1, n_2) where $n_1 \neq 0$ and $n_2 \neq 0$ known as chiral BNNTs.

Since 1992 after the discovery of nanocones, it has been observed that these structures are more attractive than carbon fullerenes, nanotubes, and nanocones researchers because of special mechanical, physical, and electronic properties [50-53]. In 1994, BN nanocones similar to carbon nanocones were suggested, and several years later, by rolling nanostructure sheet, they were synthesized [54-59].

This article has studied the interaction between the BN nanocones and the metal atoms of the first and the second groups in the periodic table using the spin-polarized density functional theory (DFT) method. In this model, the individual metal atom has been cited in the center of two kinds of single-walled B_9N_9 and $B_{40}N_{40}$ nanocones (Scheme 1a,b).

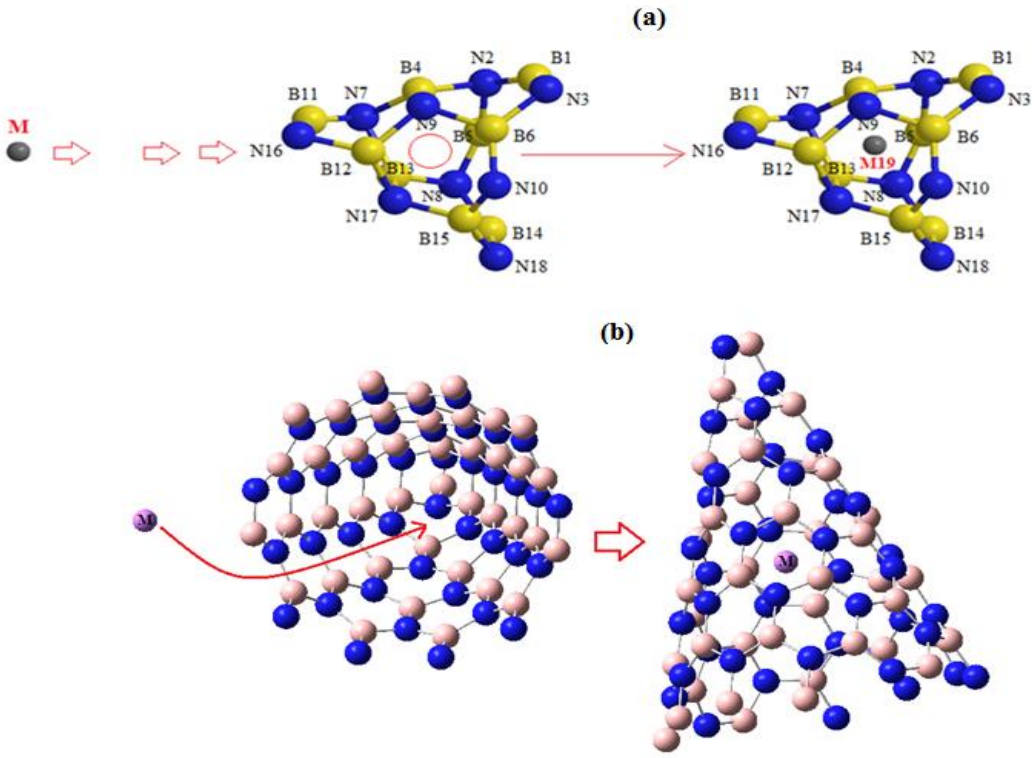

Scheme 1. Optimized structure of boron nitride nanocones of **(a)** B_9N_9 and **(b)** $B_{40}N_{40}$.

In this article, it has been investigated that the BN-metal nanocone can be applied as a biosensor for trapping and transferring the metal atoms in the biocells. Therefore, BN biosensors have been examined to indicate excellent selectivity and acceptable repeatability with a remarkable potential through a good semiconductor for sensing and detecting the metal atom in biocells aspect of different applications such as disease diagnosis, drug delivery, or cell therapy.

2. Material and Method

Hybrid functional is a group of estimations toward the exchange-correlation energy functional in DFT (Density Functional Theory), which combines a part of exact exchange from HF (Hartree–Fock theory) method with the rest of the exchange-correlation energy from other information such as empirical or ab initio methodologies. Therefore, the exact exchange energy functional is illustrated by the Kohn–Sham orbitals instead of the density, so it is placed as the indirect density functional. This study has applied the influence of the hybrid function of the three-parameter basis set of B3LYP (Becke, Lee, Yang, Parr) within the framework of DFT upon theoretical calculations [60,61]. In fact, the popular B3LYP (Becke, three-parameter, Lee–Yang–Parr) exchange-correlation functional is [62-64]:

$$E_{\mathrm{XC}}^{\mathrm{B3LYP}} = (1-\alpha)E_{\mathrm{x}}^{\mathrm{LSDA}} + \alpha E_{\mathrm{x}}^{\mathrm{HF}} + b\Delta E_{\mathrm{x}}^{\mathrm{B}} + (1-c)E_{\mathrm{c}}^{\mathrm{LSDA}} + cE_{\mathrm{c}}^{\mathrm{LYP}} \quad (1)$$

where $\alpha = 0.20, b = 0.72, c = 0.81$ is a generalized gradient approximation: the Becke exchange functional [60] and the correlation functional of Lee, Yang, and Parr [61] for B3LYP and $E_{\mathrm{c}}^{\mathrm{LSDA}}$ is the VWN local spin density approximation to the correlation functional [65].

In this work, the geometries have been optimized at the framework of DFT using basis sets of lnl2dz for transition metal cations of Li, Na, K, Be, Mg, Ca, and 6-311+G(2d,p) for B, N atoms of B_9N_9 and $B_{40}N_{40}$ nanocones. Then, it has been described the electronic structure of BN-metal atoms nanoclusters for measuring physicochemical properties (Scheme 1).

DFT theory proves an advantageous method for predicting chemical systems, and in order to understand its similarities and differences to other computational methods employed [66-68].

In this article, the Onsager model has been accomplished that was developed by Frisch, Wong, and Wiberg utilizes spherical cavities. Even though this implies a less accurate description of the solute-solvent interface, this approximation simplifies the evaluation of energy formatives in geometry optimizations and frequency analysis. Moreover, Cramer and Truhlar improved this model at the dipole level [69-74]. In fact, a cavity must have a physical sense, such as the Onsager model, and has a mathematical ability, as often happened in other descriptions of solvent impacts. The cavity has to keep out the solvent and include its frontiers as the biggest probability part of the solute charge distribution [75].

Then, The gauge consisting of atomic orbitals (GIAO) has been adopted to solve the gauge problem in the measurement of NMR shielding for the nanoclusters of $B_{40}LiN_{40}$, $B_{40}NaN_{40}$, $B_{40}KN_{40}$, $B_{40}BeN_{40}$, $B_{40}MgN_{40}$, and $B_{40}CaN_{40}$ which have trapped the metal atoms of Li, Na, K Be, Mg, Ca using density functional theory (DFT) frameworks.

A type of linkage of nanocones to metal atoms is Van der Waals forces, which depend on the distance between the atoms. In fact, VdW appears when the electron density around the nucleus of an atom undergoes a transient shift. In this article, when the electron density increases in one side of the nucleus, including N atoms, the resulting transient charge might attract or repel a neighboring atom of Li, Na, K, Be, Mg, and Ca. On the other hand, an induced formation of a dipole in BN nanocones fluctuates another dipole in trapped metal atoms in the center of nanocones.

Therefore, a group of quantum theoretical methods has been run for exploring the optimized structures of [BN-metal atoms] nanoclusters as delivering the metal atoms in the biocells through the calculations including charge distribution, NMR, NQR spectroscopy, and HOMO, LUMO molecular orbitals analysis using software of Gaussian 16 revision C.01 [76].

3. Results and Discussion

It has been observed that B vacancies, indicating N-terminated triangular holes in the lattice, could trap and encapsulate metal atoms of Li, Na, K, Be, Mg, and Ca due to the huge stability influence achieved from the Metal–N bond formation. Therefore, it has been considered the trapping site for the metal elements according to the most stable stacking configuration (Scheme 1).

3.1. Thermodynamic function analysis.

The optimized free binding energy resulting from the interaction between trapped metal atoms of Li, Na, K; Be, Mg, Ca with B_9N_9 and $B_{40}N_{40}$ nanocones has been evaluated via Eq.1 (Scheme1a,b).

$$\Delta G_b = \Delta G_{metal\text{-}BNnanocone} - (\Delta G_{metal} + \Delta G_{BN\ nanocone}) \quad (2)$$

The Gibbs free energy (G) of the nanocone clusters is computed by correcting the electronic energies (E) for the zero-point energy (ZPE), heat capacity ($\int Cp\,dT$), and the vibrational entropic term (S_{vib}) :

$$G = E + ZPE + \int Cpdt - TS_{vib} \quad (3)$$

Table 1. Calculated thermodynamic parameters of ΔG , ΔH, ΔS for B_9N_9 nanocone using DFT/EPRII,EPRIII methods at 296-304 K.

T(K)	ΔH		ΔG		ΔS	
	EPRII	EPRIII	EPRII	EPRIII	EPRII	EPRIII
296	0.0979	0.0985	-0.1983	-0.1977	0.333	0.334
298	0.2046	0.2052	-0.4117	-0.411	0.692	0.692
300	0.2968	0.2968	-0.5955	-0.5949	1.001	1.001
302	0.3972	0.3972	-0.7957	-0.7944	1.333	1.334
304	0.4976	0.4995	-0.9965	-0.9933	1.666	1.665

Table2. Calculated thermodynamic parameter of ΔG for [B_9N_9 – (Li, Na, K; Be, Mg, Ca)] nanocluster by B1LYP, B3LYP/EPRII, EPRIII, lanl2dz methods at 296-304 K.

T(K)	B1LYP						B3LYP				
	Li	Na	K	Be	Mg	Ca	Li	K	Be	Mg	Ca
296	-0.2045	-0.2083	-0.2491	-0.1945	-0.1964	-0.2278	-0.2052	-0.2497	-0.1907	-0.2064	-0.2390
298	-0.4254	-0.4330	-0.5177	-0.4041	-0.4078	-0.4737	-0.4267	-0.5189	-0.3966	-0.4298	-0.4963
300	-0.6156	-0.6269	-0.7492	-0.5854	-0.5911	-0.6858	-0.6181	-0.7517	-0.5741	-0.6225	-0.7185
302	-0.8220	-0.8371	-1.0008	-0.7818	-0.7894	-0.9161	-0.8251	-1.0034	-0.7668	-0.8320	-0.959
304	-1.0297	-1.0485	-1.2531	-0.9789	-0.9889	-1.1464	-1.0328	-1.2562	-0.9607	-1.0416	-1.2010

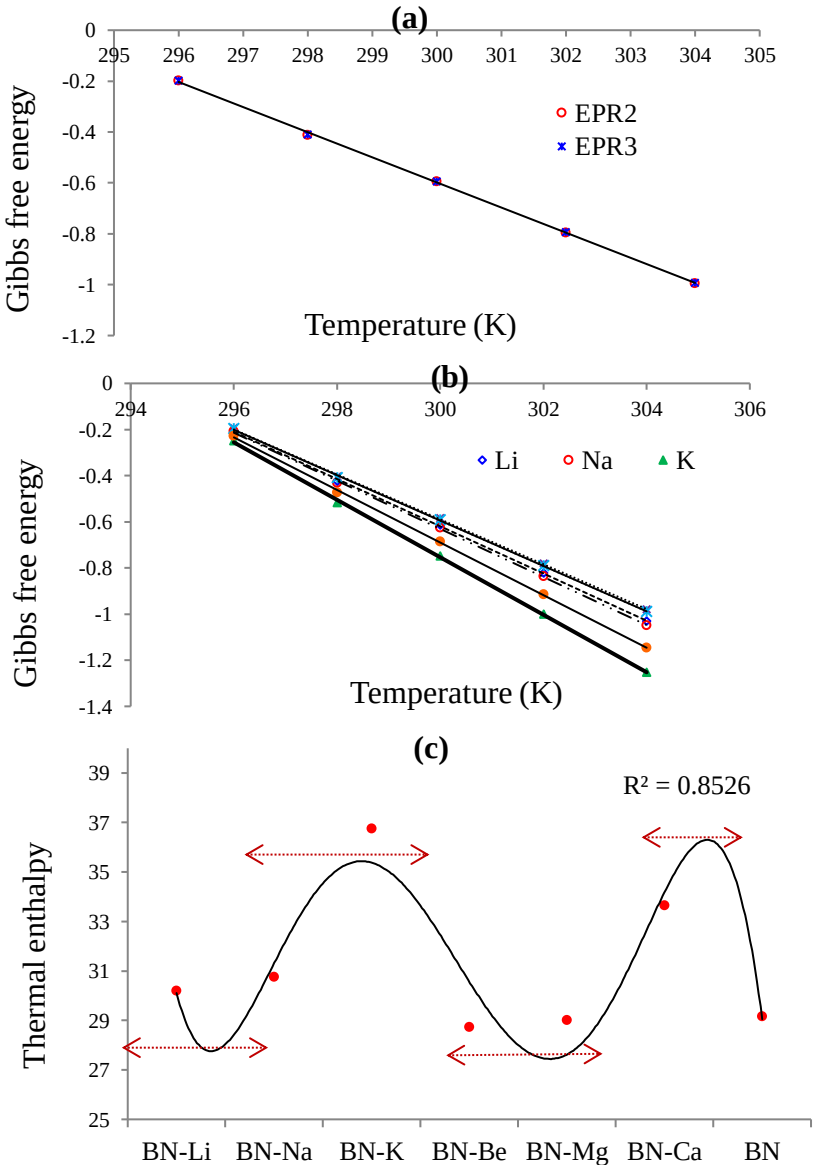

Figure 1. Calculated thermodynamic parameters of Gibbs free energy (ΔG) for **(a)** B_9N_9 nanocone **(b)**, [B_9N_9-metal ions] nanocluster and **(c)** Thermal enthalpy (ΔH) for [B_9N_9-metal ions] nanocluster, ΔS for B_9N_9 nanocone due to DFT/EPRII, EPRIII, lanl2dz methods at 296-304 K.

As a matter of fact, it has been computed the vibrational modes by analyzing a normal mode and the whole 3N degree of freedom for the metal atoms trapped in the B9N9 nanocone through the harmonic oscillator approximation.

Therefore, the theoretical studies can identify the free binding energy of a metal atom (ΔG) as a simple descriptor of the biosensor performance in semiconductor metal-BN nanocone. In fact, according to the interaction between metal atoms and BN nanocone, there is an amount of free energy that is neither too intense nor too feeble [77-82].

If the interaction is too feeble, a high over-potential will be required to trap the metal in the center of the BN nanocone. In other words, if the interaction is too strong, the metal atoms will destroy the BN nanocone. Therefore, the optimum condition is satisfied when the free binding energy is close to zero.

In this work, we have calculated the thermodynamic parameters (a.u.) such as ΔG, ΔH, ΔS of B_9N_9 nanocone and B_9N_9 trapping the metal atoms including Li, Na, K; Be, Mg, Ca using B1LYP, B3LYP levels of theory and basis sets of EPRII, EPRIII for B, N atoms and lanl2dz for metal atoms at different temperature of 296, 298, 300, 302 and 304 K (Tables 1&2 and Figure 1a-c).

Figure 1a,b has illustrated that the variation of Gibbs free energy behaves as a linear relationship observed between temperature and ΔS, which decrease with increasing the temperature from 296-304K for B_9N_9 nanocone ($R^2 \approx 0.9998$) and [B_9N_9-metal atoms] ($R^2 = 0.9996$) nanocluster based on the Eqs. 4-10:

$$\Delta G_{B9N9\ nanocone} = -0.0992T_{B9N9\ nanocone} + 29.147 \quad (4)$$

$$\Delta G_{(Li)} = -0.1027T_{(Li)} + 30.2 \quad (5) \quad ; \quad \Delta G_{(Na)} = -0.1046T_{(Na)} + 30.754 \quad (6)$$

$$\Delta G_{(K)} = -0.125T_{(K)} + 36.757 \quad (7) \quad ; \quad \Delta G_{(Be)} = -0.0977T_{(Be)} + 28.717 \quad (8)$$

$$\Delta G_{(Mg)} = -0.0987T_{(Mg)} + 29.007 \quad (9) \quad ; \quad \Delta G_{(Ca)} = -0.1144T_{(Ca)} + 33.637 \quad (10)$$

Then, it has been evaluated whether there is a thermal enthalpy cost or gains to go from a B_9N_9 nanocone and trap a single metal atom to form the [B_9N_9-metal atoms] nanocluster, which has been plotted in Figure 1c.

Moreover, the changes of reaction enthalpy of ΔH_R among [$B_{40}N_{40}$- (Li, Na, K; Be, Mg, Ca)] nanoclusters have been explored through interaction between $B_{40}N_{40}$ nanocone and metal atoms that illustrates the stability of these complexes through the differences among the thermal enthalpy of formation of $B_{40}MN_{40}$ nanocluster, $B_{40}N_{40}$ nanocone and metal atoms including Li, Na, K; Be, Mg, Ca as Eq.10 as follows (Table 3& Figure 2a,b):

$$\Delta H_R = \Delta H_{f,\ B40MN40} - (\Delta H_{f,\ Metal} + \Delta H_{f,\ B40N40}) \quad (11)$$

Table3. Calculated the thermal enthalpy (ΔH_f /kcal.mol^{-1}) for Metal atom, B40N40, B40MN40 and thermal reaction (ΔH_R /kcal.mol^{-1})of B40N40- (Li, Na, K; Be, Mg, Ca) nanoclusters due to B3LYP/ 6-311+G (d, p), lanl2dz methods.

Metal-$B_{40}N_{40}$ nanocone	$\Delta H_{f,\ B40N40}$	Metal	$\Delta H_{f,\ Metal} \times 10^{-3}$	$\Delta H_{f,\ B40MN40} \times 10^{-4}$	$\Delta H_R \times 10^{-4}$
$B_{40}LiN_{40}$	-412.3545×10^{-4}	Li	-4.477	-196.7255	216.0767
$B_{40}NaN_{40}$		Na	-100.264	-206.3002	216.0807
$B_{40}KN_{40}$		K	-372.113	-233.4863	216.0795
$B_{40}BeN_{40}$		Be	-8.433	-197.1434	216.0544
$B_{40}MgN_{40}$		Mg	-123.311	-208.6127	216.0729
$B_{40}CaN_{40}$		Ca	-420.069	-238.2902	216.0712

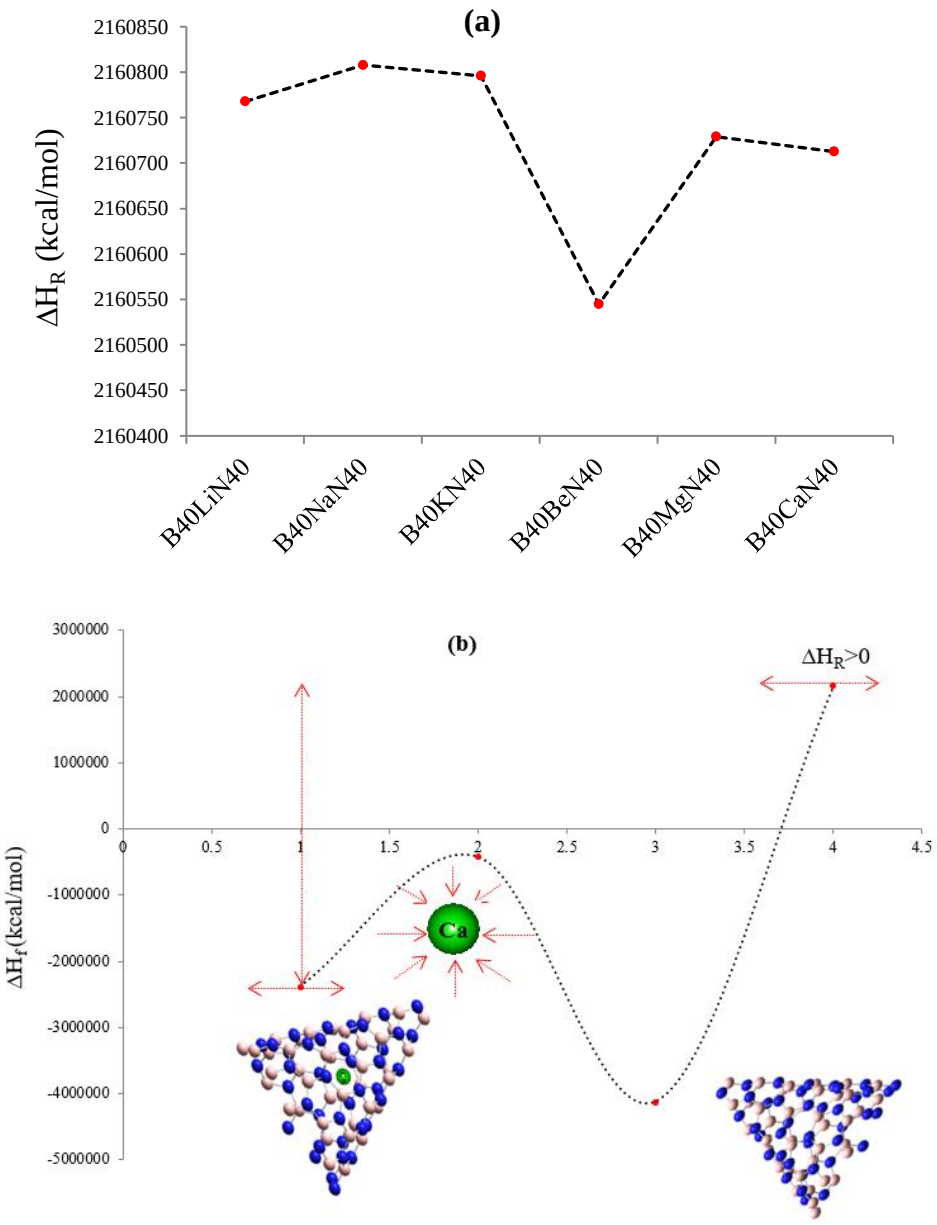

Figure 2. (a) Calculated graph of heat reaction (ΔH_R) for $B_{40}MN_{40}$ (M=Li, Na, K/Be, Mg, Ca). **(b)** The mechanism for the formation of $B_{40}CaN_{40}$ from Ca metal atom and $B_{40}N_{40}$ nanocone due to heat formation of each component.

The highest trapping stability with different metal atoms indicates that $B_{40}N_{40}$ nanocone can produce a variety of nanoclusters, including $B_{40}MN_{40}$ nanoclusters (M=Li, Na, K; Be, Mg, Ca) (Figure 2a,b).

It is possible to make a correlation between biosensor activity and thermodynamic properties, which can be calculated by density functional theory (DFT) and basis sets of EPRII, EPRIII, 6-311+G (d, p) for B, N atoms, and lanl2dz for metal atoms of Li, Na, K; Be, Mg, Ca, respectively. This calculation has allowed a rationalization of the reactivity trends among different metal atoms, which can identify and predict potential novel semiconductors as biosensors in the biocells.

3.2. NMR spectroscopy in B40N40.

The results of NMR spectroscopy in Figure 3 have shown that nanoclusters of $B_{40}MN_{40}$ present chemical shielding between 0-275 ppm for $B_{40}LiN_{40}$, 0-600 ppm for $B_{40}NaN_{40}$, 0-1300

ppm for $B_{40}KN_{40}$, 0-275 ppm for $B_{40}BeN_{40}$, 0-680 ppm for $B_{40}MgN_{40}$, and 0-1400 ppm for $B_{40}CaN_{40}$.

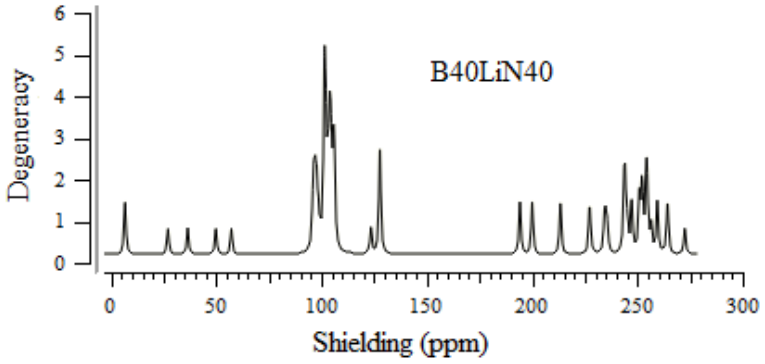

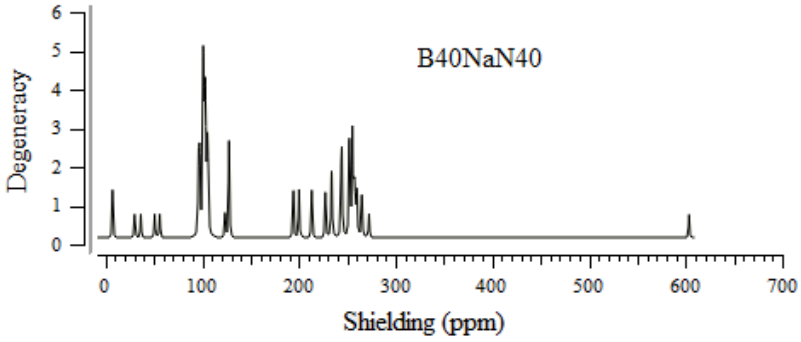

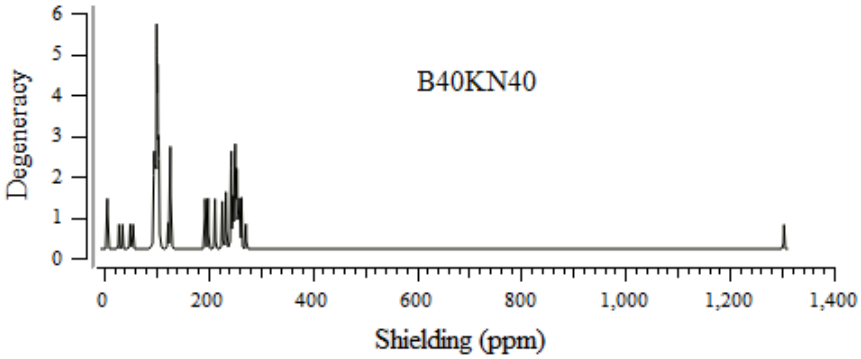

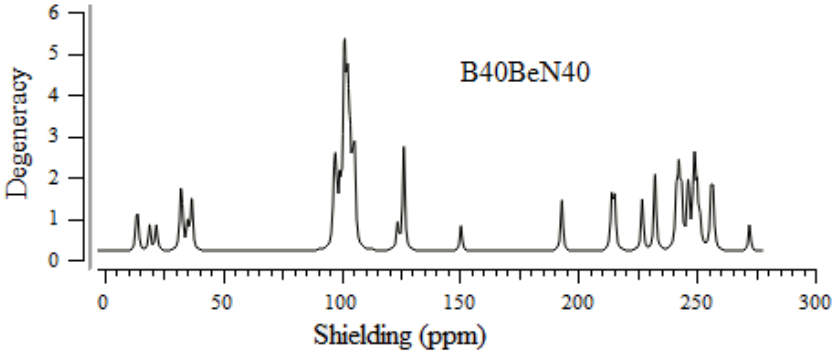

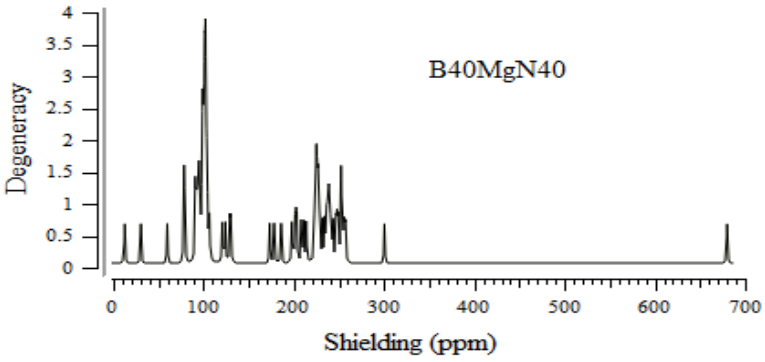

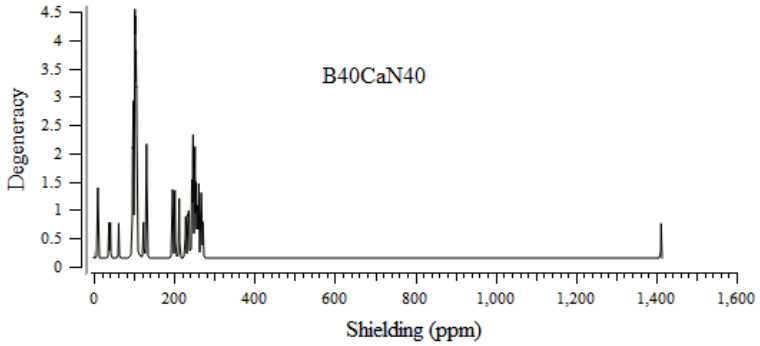

Figure3. NMR spectra of trapped $B_{40}LiN_{40}$, $B_{40}NaN_{40}$, $B_{40}KN_{40}$, $B_{40}BeN_{40}$, $B_{40}MgN_{40}$, and $B_{40}CaN_{40}$ in different ranges of chemical shielding in ppm.

The sharpest peak of the NMR spectrum has been almost observed in 100 ppm for all of the $B_{40}MN_{40}$ nanoclusters, including $B_{40}LiN_{40}$, $B_{40}NaN_{40}$, $B_{40}KN_{40}$, $B_{40}BeN_{40}$, $B_{40}MgN_{40}$, and $B_{40}CaN_{40}$. On the other hand, the weakest peaks of the NMR spectrum have approximately appeared in 250 ppm for all six $B_{40}MN_{40}$ nanoclusters (M=Li, Na, K; Be, Mg, Ca) (Figure 3).

The parameters of isotropic shielding tensor (CSI), anisotropic shielding tensor (CSA), and eigenvalues of chemical shielding, including σ_{11}, σ_{22}, σ_{33} resulted from NMR data $B_{40}LiN_{40}$, $B_{40}NaN_{40}$, $B_{40}KN_{40}$, $B_{40}BeN_{40}$, $B_{40}MgN_{40}$, and $B_{40}CaN_{40}$, respectively, have been reported in Table4. The calculated results indicated the SCF GIAO magnetic shielding tensor in ppm and charge transfer for Li, Na, K; Be, Mg, and Ca trapped into the B40N40 nanocone as the transfer target releasing the metal atoms in the biocells. The computations have been accomplished based on B3LYP/6-311+G (2d,p), lanl2dz level of theory by software of Gaussian 16 revision C.01 (Table 4).

Table4. Optimized SCF GIAO magnetic shielding tensor and charge transfer of Li, Na, K; Be, Mg, Ca trapped into $B_{40}N_{40}$ nanocone.

Metal-$B_{40}N_{40}$ nanocone	σ_{11}	σ_{22}	σ_{33}	CSI	CSA
$B_{40}LiN_{40}$	93.4294	100.2879	102.2961	98.6712	5.4374
$B_{40}NaN_{40}$	601.4262	601.7712	607.604	603.6004	6.0053
$B_{40}KN_{40}$	1287.9519	1307.4542	1317.0696	1304.1586	19.3665
$B_{40}BeN_{40}$	147.0091	150.4528	154.1357	150.5325	5.4048
$B_{40}MgN_{40}$	668.0806	677.7494	694.5027	680.1109	21.5877
$B_{40}CaN_{40}$	1396.1215	1414.085	1426.2457	1412.1508	21.1425

CSI (ppm) = $(\sigma_{33}+\sigma_{22}+\sigma_{11})/3$; CSA (ppm) = $\sigma_{33}-(\sigma_{22}+\sigma_{11})/2$

Quantum chemical methods introduce the chemical shift tensors in the principal axes system to evaluate the two parameters CSI (isotropic chemical-shielding) and CSA (anisotropic chemical-shielding) (Figure4a,b) [83,84]:

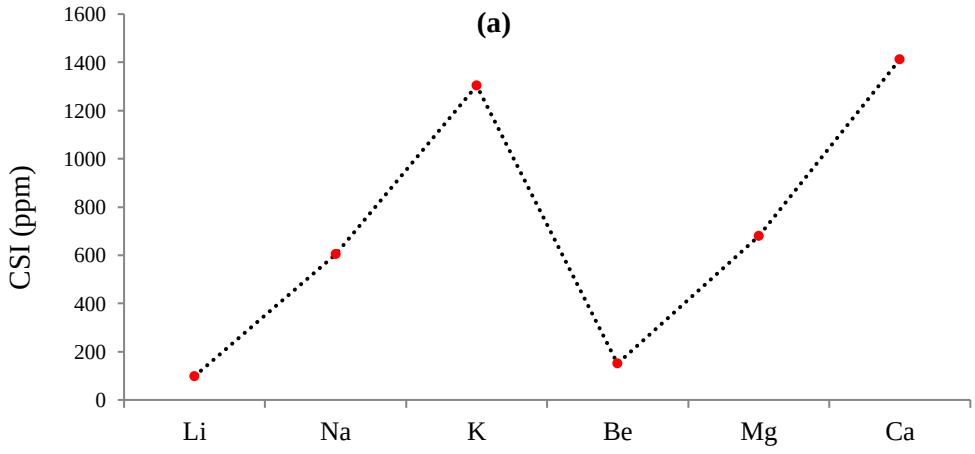

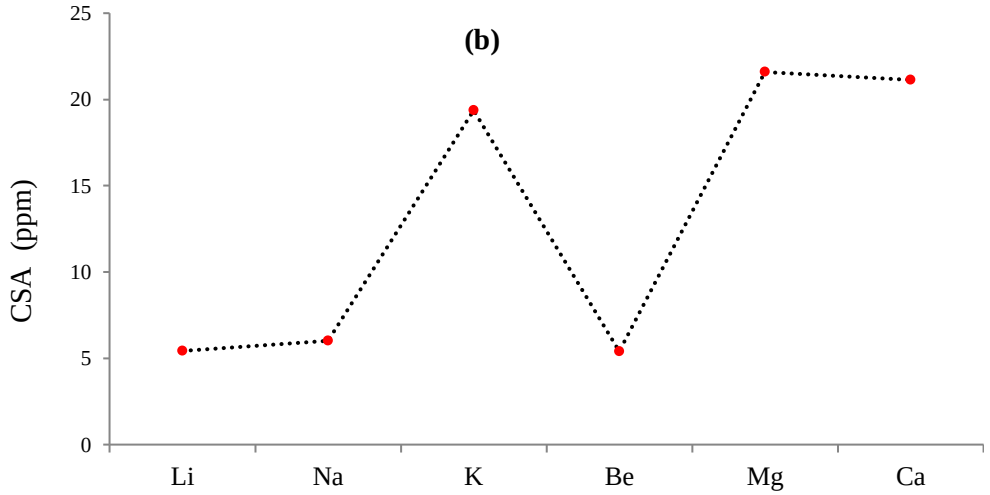

Figure 4. Calculated NMR parameters of **(a)** CSI and **(b)** CSA of metal atoms of Li, Na, K; Be, Mg, Ca trapped into the $B_{40}N_{40}$ nanocone by B3LYP/6-311+G(2d,p), lanl2dz level of theory.

Figure 4 indicates the fluctuation of chemical shielding tensors of CSI and CSA for different metal atoms, which declare the stability of [$B_{40}N_{40}$- (Li, Na, K; Be, Mg, Ca)] nanoclusters.

3.3. Atomic charge diffusion and nuclear quadrupole resonance.

The optimized atomic charge (Q) of Li, Na, K, Be, Mg, and Ca atoms using B3LYP/LANL2DZ,6-311+G (d, p) of theoretical level in a polar medium of water solution indicates the stability of $B_{40}LiN_{40}$, $B_{40}NaN_{40}$, $B_{40}KN_{40}$, $B_{40}BeN_{40}$, $B_{40}MgN_{40}$, and $B_{40}CaN_{40}$, respectively (Table 5, Figure 5a). In fact, it has exhibited the region includes the attractive–repulsive force of a fixed charge at different points in space that are parallel to the molecular surface of $B_{40}MN_{40}$ nanoclusters (Figure 5a).

Table 5. Calculated atomic charge and electrical potential for $B_{40}LiN_{40}$, $B_{40}NaN_{40}$, $B_{40}KN_{40}$, $B_{40}BeN_{40}$, $B_{40}MgN_{40}$ nanoclusters using B3LYP/6-311+G (2d,p), lanl2dz.

Nanocone-Metal ion	Q	Electrical potential
B40LiN40	0.4953	-5.3867
B40NaN40	0.8899	-34.3245
B40KN40	0.6432	-74.0244
B40BeN40	-0.1432	-8.3914
B40MgN40	1.2668	-38.6413
B40CaN40	1.2292	-79.0276

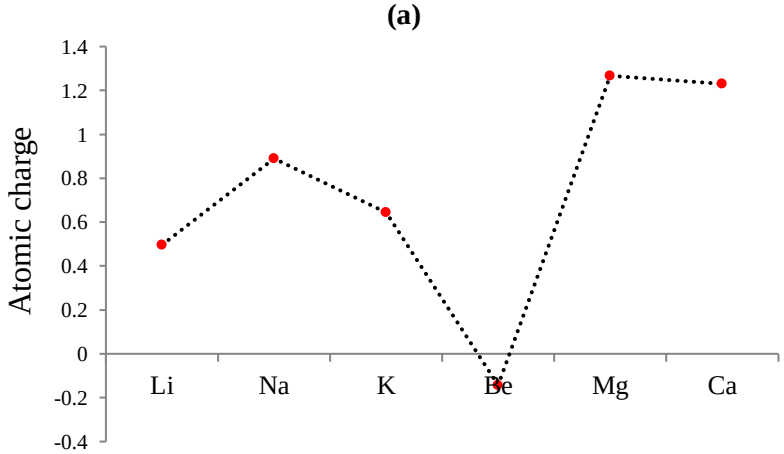

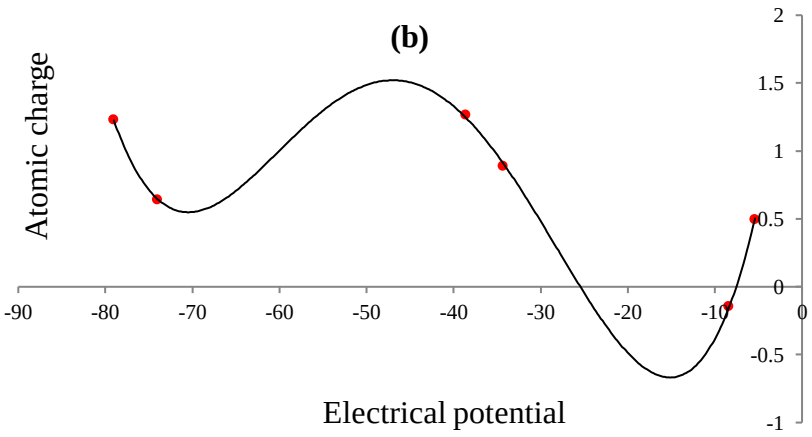

Figure 5. (a) The optimized atomic charge (Q) of Li, Na, K, Be, Mg, Ca atoms using B3LYP/LANL2DZ,6-311+G (d, p) of theoretical level in a polar medium of water solution. **(b)**The polynomial graph (order=4) of atomic charge versus the electric potential of $B_{40}LiN_{40}$, $B_{40}NaN_{40}$, $B_{40}KN_{40}$, $B_{40}BeN_{40}$, $B_{40}MgN_{40}$, and $B_{40}CaN_{40}$ encapsulating Li, Na, K, Be, Mg, Ca by B3LYP/6-311+G (2d,p) method.

It has been recommended the reason for the existing stability of [$B_{40}N_{40}$- (Li, Na, K; Be, Mg, Ca)] nanoclusters which indicate the position of active sites of metal atoms trapped into nanocone of $B_{40}N_{40}$ by moving the charge of electrons in these compounds in polar water molecules (Figure 5a). In other words, the electrophilic side chains of metal atoms of Li, Na, K; Be, Mg, and Ca conduct us to find the reason for the activity and the stability of these nanoclusters as biosensors for transferring and releasing the metal atoms in the biocells.

Moreover, ^{14}N - NQR or nuclear quadrupole resonance approach has been accomplished for achieving the electric potential of metal atoms (Li, Na, K, Be, Mg, Ca) trapped in $B_{40}N_{40}$ nanocone using B3LYP/6-311+G (2d,p) level (Table 5).

In NMR, nuclei with spin ≥ 1/2 have a magnetic dipole moment so that their energies are split by a magnetic field, permitting resonance sorption of energy dependent on the Larmor frequency; $\omega_L = \gamma B$, where γ is the gyromagnetic ratio, and B is the magnetic field external to the nucleus.

In NQR nuclei with spin ≥ 1, there is an electric quadrupole moment which is accompanied by non-spherical nuclear charge distributions. So, the nuclear charge distribution deviates from that of a sphere as the oblate or prolate form of the nucleus. NQR is a straight frame of the interaction of the quadrupole moment with the local electric field gradient (EFG) produced by its ambiance's electronic structure. Therefore, the NQR transition frequencies are symmetric to the electric quadrupole moment of the nucleus and a measure of the strength of the local EFG:

$$\omega \sim \frac{e^2\, Qq}{\hbar} = C_q, \quad (12)$$

where q is dependent on the biggest fundamental portion of the EFG tensor at the nucleus, and C_q is quadrupole coupling constant parameter [85,86].

The NQR method is based on the multipole expansion in Cartesian coordinates as the following equations:

$$V(r) = V(0) + \left[\left(\frac{\partial V}{\partial x_i}\right)\Big|_0 . x_i\right] + \frac{1}{2}\left[\left(\frac{\partial^2 V}{\partial x_i x_j}\right)\Big|_0 . x_i x_j\right] + \cdots \quad (13)$$

Then, after simplification of the equation, there are only the second derivatives dependent on the same variable for the potential energy [85,86]:

$$U = -\frac{1}{2}\int_{\mathcal{D}} d^3 r\, \rho_r \left[\left(\frac{\partial^2 V}{\partial x_i^2}\right)\Big|_0 . x_i^2\right] = -\frac{1}{2}\int_{\mathcal{D}} d^3 r\, \rho_r \left[\left(\frac{\partial E_i}{\partial x_i}\right)\Big|_0 . x_i^2\right] =$$

$$-\frac{1}{2}\left(\frac{\partial E_i}{\partial x_i}\right)\Big|_0 . \int_{\mathcal{D}} d^3 r\, [\rho(r) . x_i^2] \quad (14)$$

There are two parameters that must be obtained from NQR experiments; the quadrupole coupling constant, χ, and the asymmetry parameter of the EFG tensor η:

$$\chi = e^2 Q q_{zz} / h ; \quad (15)$$

$$\eta = (q_{xx} - q_{yy}) / q_{zz} \quad (16)$$

where q_{ii} are components of the EFG tensor at the quadrupole nucleus determined in the EFG principal axes system, Q is the nuclear quadrupole moment, e is the proton charge, and h is Planck's constant [87].

In Figure 5b, it has been observed the polynomial graph (order=4) of atoms $B_{40}LiN_{40}$, $B_{40}NaN_{40}$, $B_{40}KN_{40}$, $B_{40}BeN_{40}$, $B_{40}MgN_{40}$, and $B_{40}CaN_{40}$ encapsulating Li, Na, K, Be, Mg, Ca with relation coefficient of R^2= 0.9993 due to atomic charge versus electric potential which has been achieved by B3LYP/6-311+G (2d,p) method.

3.4. Frontier molecular orbital of HOMO and LUMO.

The electron affinity produces LUMO, or the lowest unoccupied molecular orbital energy, and the ionization makes HOMO, or the highest occupied molecular orbital energy which has been measured and introduced for $B_{40}MN_{40}$ nanoclusters (Table 6). The HOMO, LUMO, and band energy gap (eV) remarked the figurative description of the frontier molecular orbital's and their relative positive and negative districts, which are substantial operators for recognizing the molecular specifications of $B_{40}MN_{40}$ nanoclusters (Scheme2).

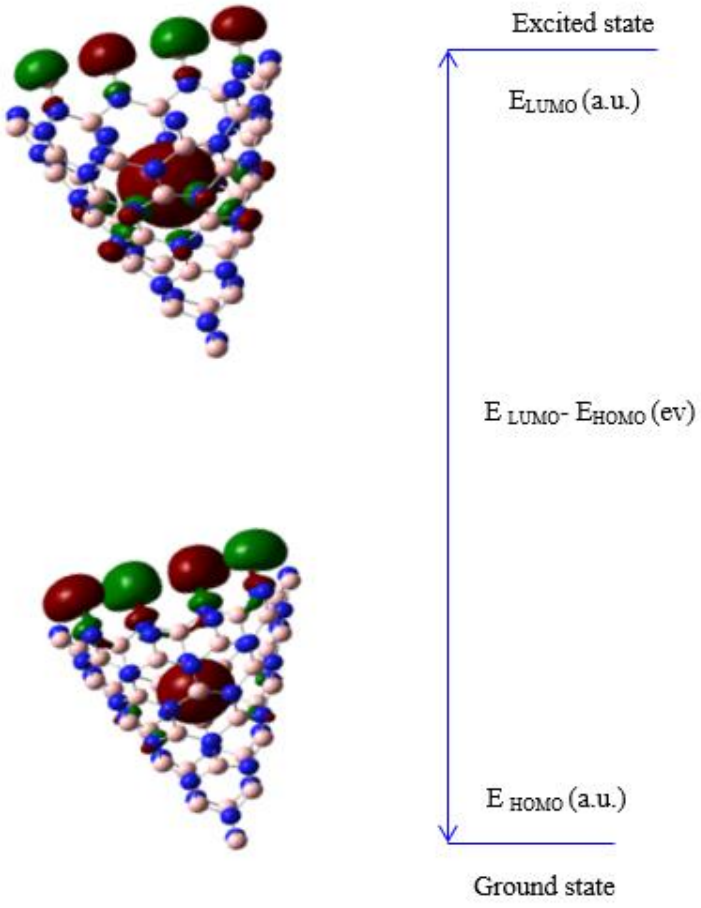

Scheme 2. The HOMO (a.u.), LUMO (a.u.), and band energy gap (eV) for $B_{40}MN_{40}$ nanoclusters.

The HOMO displays the susceptibility for giving an electron, while the LUMO, an electron acceptor, depicts the ability to get an electron. In fact, the energy gap (ΔE = E LUMO-EHOMO) demonstrates the energy difference between frontier HOMO and LUMO orbital representing the structure's resistance and appears the compound's chemical activity. In this work, the energy gap assigns how $B_{40}N_{40}$ traps metal atoms of Li, Na, K, Be, Mg, and Ca. In addition, the frontier molecular orbitals operate an important function in the optical and electrical properties like in UV-Vis spectra [88].

Figure 6 demonstrates the changes of energy gap (E_{LUMO} - E_{HOMO}) versus effective biosensors of [$B_{40}N_{40}$ - metal atoms] clusters containing $B_{40}LiN_{40}$, $B_{40}NaN_{40}$, $B_{40}KN_{40}$, $B_{40}BeN_{40}$, $B_{40}MgN_{40}$, and $B_{40}CaN_{40}$ at B3LYP/6-311+G(2d,p),lanl2dz level of theory with The polynomial graph (order=3) and relation coefficient of $R^2 = 0.8853$.

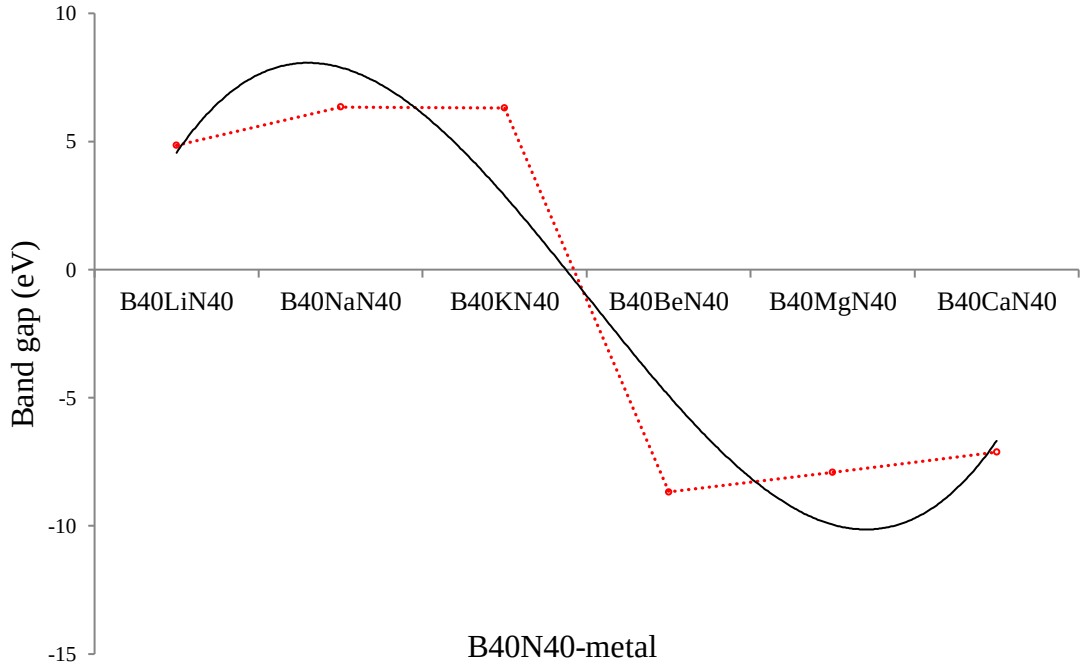

Figure 6. The band gap (eV) of HOMO-LUMO for [$B_{40}N_{40}$ - metal atoms] clusters.

Moreover, to get more conclusive approval in identifying the characteristics of $B_{40}MN_{40}$ nanoclusters, a series of chemical reactivity parameters such as chemical potential (μ), electronegativity (χ), hardness (η), softness (ζ), electrophilicity index (ψ) has been carried out (Table 6) [89-91].

Table 6. The HOMO, LUMO, band energy gap, chemical potential (μ), electronegativity (χ), hardness (η), softness (ζ), electrophilicity index (ψ) (eV) have been accomplished using the following equations for $B_{40}MN_{40}$ nanoclusters.

Compound quantities (ev)	B40LiN40	B40NaN40	B40KN40	B40BeN40	B40MgN40	B40CaN40
E_{HOMO}	-6.2863	-6.4387	-6.3163	-9.8682	-8.9392	-8.6154
E_{LUMO}	-1.4460	-0.0990	-0.0049	-7.4793	-6.8749	-5.6240
ΔE	4.8403	6.3397	6.3114	2.3889	2.0643	2.9914
μ	-3.8661	-3.2688	-3.1606	-8.6737	-7.9070	-7.1197
χ	3.8661	3.2688	3.1606	8.6737	7.9070	7.1197
η	2.4201	3.1698	3.1557	1.1944	1.0321	1.4957
ζ	0.2066	0.1577	0.1584	0.4186	0.4844	0.3343
ψ	3.0880	1.6855	1.5827	31.4931	30.2870	16.9453

ΔE= E_{LUMO}- E_{HOMO} ; $\mu=(E_{HOMO}+E_{LUMO})/2$; $\chi= -(E_{HOMO}+E_{LUMO})/2$; $\eta = (E_{LUMO} -E_{HOMO})/2$; $\zeta =1/(2\eta)$; $\psi = \mu^2/(2\eta)$

The compound quantities parameters in Table 6 have displayed a good resistance for $B_{40}MN_{40}$ nanoclusters consisting of $B_{40}LiN_{40}$, $B_{40}NaN_{40}$, $B_{40}KN_{40}$, $B_{40}BeN_{40}$, $B_{40}MgN_{40}$, and $B_{40}CaN_{40}$ through applying as biosensors in transferring and releasing the metal atoms in the biocells.

4. Conclusions

A selective biosensor of B_9N_9 and $B_{40}N_{40}$ trapping the metal atoms of Li, Na, K, Be, Mg, and Ca has been recommended, which might be applied for boron nitride, detecting different reactions in the biocells. The molecular geometry of the compounds in the ground state has been computed using B3LYP// EPRII, EPRIII/ 6-311+G (d, p)/ lanl2dz methods for obtaining several physical and chemical parameters.

Then, charge distribution, NMR, and NQR analysis on [BN-metal atoms] nanoclusters have been performed using B3LYP// EPRII, EPRIII/ 6-311+G (d, p)/ lanl2dz methods. Besides, the HOMO-LUMO energy gap is supported in analyzing the chemical reactivity of the molecule. NMR calculations have indicated a strong effect for the most intense peak predicted in the case of the [BN-metal atoms] nanoclusters.

The Fourth-order perturbation analysis of the NQR spectrum has been performed to investigate the effect of the metal atoms' coordination on the different interactions within the studied molecules.

The outcomes of the above perceptions can recommend that the various data gained from $B_{40}MN_{40}$ nanoclusters consisting of $B_{40}LiN_{40}$, $B_{40}NaN_{40}$, $B_{40}KN_{40}$, $B_{40}BeN_{40}$, $B_{40}MgN_{40}$, and $B_{40}CaN_{40}$ in the solvent is mainly because of basis set functions which are derived by a shift in the polarization of the ambiance. Notably, growth in the dielectric constants raises the resistance and turnover of these $B_{40}MN_{40}$ nanoclusters for application as biosensors in transferring and releasing the metal atoms in the biocells.

Funding

This research received no external funding.

Acknowledgments

In successfully completing this paper and the research behind it, the corresponding author is grateful to all of the authors for their pretty helpful contributions.

Conflicts of Interest

The authors declare no conflict of interest.

References

1. Yoon, B.; Choi, S.-J.; Swager, T.M.; Walsh, G.F. Flexible Chemiresistive Cyclohexanone Sensors Based on Single-Walled Carbon Nanotube–Polymer Composites. *ACS Sens*. **2021**, *6*, 3056–3062, https://doi.org/10.1021/acssensors.1c01076.
2. Mollaamin, F.; Monajjemi, M. Harmonic Linear Combination and Normal Mode Analysis of Semiconductor Nanotubes Vibrations. *J. Comput. Theor. Nanosci* **2015**, *12*, 1030-1039, https://doi.org/10.1166/jctn.2015.3846.
3. Wu, Y.; Zhao, X.; Shang, Y.; Chang, S.; Dai, L.; Cao, A. Application-Driven Carbon Nanotube Functional Materials. *ACS Nano* **2021**, *15*, 7946–7974, https://doi.org/10.1021/acsnano.0c10662.

4. Monajjemi, M.; Mahdavian, L.; Mollaamin, F.; Khaleghian, M. Interaction of Na, Mg, Al, Si with carbon nanotube (CNT): NMR and IR study. *Russ. J. Inorg. Chem* **2009**, *54*, 1465-1473, https://doi.org/10.1134/S0036023609090216.
5. Pandhi, T.; Chandnani, A.; Subbaraman, H.; Estrada, D. A Review of Inkjet Printed Graphene and Carbon Nanotubes Based Gas Sensors. *Sensors* **2020**, *20*, 5642, https://doi.org/10.3390/s20195642.
6. Mahdavian, L.; Monajjemi, M. Alcohol sensors based on SWNT as chemical sensors: Monte Carlo and Langevin dynamics simulation. *Microelectronics journal* **2010**, *41*, 142-149, https://doi.org/10.1016/j.mejo.2010.01.011.
7. Monajjemi, M.; Najafpour, J.; Mollaamin, F. $(3,3)_4$ Armchair carbon nanotube in connection with PNP and NPN junctions: Ab Initio and DFT-based studies. *Fullerenes Nanotubes and Carbon Nanostructures* **2013**, *21*, 213-232, https://doi.org/10.1080/1536383X.2011.597010.
8. Bezdek, M.J.; Luo, S.X.L.; Liu, R.Y.; He, Q.; Swager, T.M. Trace Hydrogen Sulfide Sensing Inspired by Polyoxometalate-Mediated Aerobic Oxidation. *ACS Cent. Sci.* **2021**, *7*, 1572–1580, https://doi.org/10.1021/acscentsci.1c00746.
9. Liu, C.; Hu, J.; Wu, G.; Cao, J.; Zhang, Z.; Zhang, Y. Carbon Nanotube-Based Field-Effect Transistor-Type Sensor with a Sensing Gate for Ppb-Level Formaldehyde Detection. *ACS Appl. Mater. Interfaces* **2021**, *13*, 56309–56319, https://doi.org/10.1021/acsami.1c17044.
10. Monajjemi, M.; Mollaamin, F.; Gholami, M.R.; Yoosbashizadeh, H.; Sadrnezhad, S.K.; Passdar, H. Quantum Chemical Parameters of Some Organic Corrosion Inhibitors, Pyridine, 2-Picoline 4-Picoline and 2,4-Lutidine, Adsorption at Aluminum Surface in Hydrochloric and Nitric Acids and Comparison Between Two Acidic Media. *Main Group Met. Chem.* **2003**, *26*, 349-362, https://doi.org/10.1515/MGMC.2003.26.6.349.
11. Shkodra, B.; Petrelli, M.; Costa Angeli, M.A.; Garoli, D.; Nakatsuka, N.; Lugli, P.; Petti, L. Electrolyte-gated carbon nanotube field-effect transistor-based biosensors: Principles and applications. *Appl. Phys. Rev.* **2021**, *8*, 041325, https://doi.org/10.1063/5.0058591.
12. Yu, H.; Luo, H.; Cai, J.; Dong, C. Molecular and atomic adsorptions of hydrogen, oxygen, and nitrogen on defective carbon nanotubes: A first-principles study. *Int. J. Hydrog. Energy* **2020**, *45*, 26655–26665, https://doi.org/10.1016/j.ijhydene.2020.07.039.
13. Agarwal, P.B.; Sharma, R.; Mishra, D.; Thakur, N.K.; Agarwal, A.; Ajayaghosh, A. Silicon Shadow Mask Technology for Aligning and in Situ Sorting of Semiconducting SWNTs for Sensitivity Enhancement: A Case Study of NO2 Gas Sensor. *ACS Appl. Mater. Interfaces* **2020**, *12*, 40901–40909, https://doi.org/10.1021/acsami.0c10189.
14. Zhou, T.; Zhang, T. Recent Progress of Nanostructured Sensing Materials from 0D to 3D: Overview of Structure–PropertyApplication Relationship for Gas Sensors. *Small Methods* **2021**, *5*, 2100515, https://doi.org/10.1002/smtd.202100515.
15. Monajjemi, M.; Khaleghian, M.; Tadayonpour, N.; Mollaamin, F. The effect of different solvents and temperatures on stability of single-walled carbon nanotube: A QM/MD study, *Int. J. Nanosci.* **2010**, *09*, 517-529, https://doi.org/10.1142/S0219581X10007071.
16. Lee, S.-H.; Kim, M.J.; Ahn, S.; Koh, B. Purification of Boron Nitride Nanotubes Enhances Biological Application Properties. *Int. J. Mol. Sci.* **2020**, *21*, 1529, https://doi.org/10.3390/ijms21041529.
17. Knobloch, T.; Illarionov, Y.; Ducry, F.; Schleich, C.; Wachter, S.; Watanabe, K.; Taniguchi, T.; Mueller, T.; Waltl, M.; Lanza, M.; et al. The performance limits of hexagonal boron nitride as an insulator for scaled CMOS devices based on two-dimensional materials. *Nat. Electron.* **2021**, *4*, 98–108, https://doi.org/10.1038/s41928-020-00529-x.
18. Gao, X.; Yao, Y.; Meng, X. Recent development on BN-based photocatalysis: A review. *Mater. Sci. Semicond. Process.* **2020**, *120*, 105256, https://doi.org/10.1016/j.mssp.2020.105256.
19. Mollaamin, F.; Monajjemi, M.; Salemi, S.; Baei, M.T. A Dielectric Effect on Normal Mode Analysis and Symmetry of BNNT Nanotube. *Fuller. Nanotub. Carbon Nanostructures* **2011**, *19*, 182-196, https://doi.org/10.1080/15363831003782932.
20. Ding, H.; Guan, J.; Lu, P.; Mihailov, S.J.; Kingston, C.T.; Simard, B. Boron nitride nanotubes for optical fiber chemical sensing applications. *IEEE Sens. Lett.* **2020**, *4*, 1–4, https://doi.org/10.1109/LSENS.2020.3023702.
21. Yanar, N.; Yang, E.; Park, H.; Son, M.; Choi, H. Boron nitride nanotube (BNNT) membranes for energy and environmental applications. *Membranes* **2020**, *10*, 430, https://doi.org/10.3390/membranes10120430.

22. Monajjemi, M.; Jafari Azan, M.; Mollaamin, F. Density functional theory study on B30N20 nanocage in structural properties and thermochemical outlook. *Fullerenes Nanotubes and Carbon Nanostructures* **2013**, *21*, 503-515, https://doi.org/10.1080/1536383X.2011.629762.
23. Jiang, X.; Ban, C.; Li, L.; Chen, W.; Liu, X. Research on ohmic contact characteristics of single boron nitride nanoribbon. *J. Nanopart. Res.* **2021**, *23*, 242, https://doi.org/10.1007/s11051-021-05358-3.
24. Mollaamin, F and Monajjemib, M. Molecular modelling framework of metal-organic clusters for conserving surfaces: Langmuir sorption through the TD-DFT/ONIOM approach. MOLECULAR SIMULATION 2022, 1-12. https://doi.org/10.1080/08927022.2022.2159996.
25. Panigrahi, P.; Kumar, A.; Bae, H.; Lee, H.; Ahuja, R.; Hussain, T. Capacity enhancement of polylithiated functionalized boron nitride nanotubes: An efficient hydrogen storage medium. *Phys. Chem. Chem. Phys.* **2020**, *22*, 15675–15682, https://doi.org/10.1039/D0CP01237H.
26. Khalili, N.P.; Moradi, R.; Kavehpour, P.; Islamzada, F. Boron nitride nanotube clusters and their hybrid nanofibers with polycaprolacton: Thermo-pH sensitive drug delivery functional materials. *Eur. Polym. J.* **2020**, *127*, 109585, https://doi.org/10.1016/j.eurpolymj.2020.109585.
27. Monajjemi, M.; Bagheri, S.; Moosavi, M.S. *et al*. Symmetry breaking of $B_2N^{(-,0,+)}$: An aspect of the electric potential and atomic charges. *Molecules* **2015**, *20*, 21636-21657, https://doi.org/10.3390/molecules201219769.
28. Lee, S.H.; Kim, M.J.; Ahn, S.; Koh, B. Purification of boron nitride nanotubes enhances biological application properties. *Int. J. Mol. Sci.* **2020**, *21*, 1529, https://doi.org/10.3390/ijms21041529.
29. Joy, J.; George, E.; Haritha, P.; Thomas, S.; Anas, S. An overview of boron nitride based polymer nanocomposites. *J. Polym. Sci.* **2020**, 55, 3115–3141, https://doi.org/10.1002/pol.20200507.
30. Maurya, M.; Sappidi, P.K.; Singh, J.K. Selective Separation of CO2 from Flue Gas Using Carbon and Boron Nitride Nanotubes as a Membrane. *Energy Fuels* **2020**, *34*, 7223–7231, https://doi.org/10.1021/acs.energyfuels.0c00311.
31. Monajjemi, M.; Lee, V. S.; Khaleghian, M.; Honarparvar, B.; Mollaamin, F. Theoretical Description of Electromagnetic Nonbonded Interactions of Radical, Cationic,And Anionic NH2BHNBHNH2 Inside of the B18N18 Nanoring. *J. Phys. Chem. C.* **2010**, *114*, 15315–15330, https://doi.org/10.1021/jp104274z.
32. Marko, Š.; Snežana, M.; Marijana K., I.; Jasmina, N.; Malcolm, W.; Zoltan, K.; Jelena, T. Comparing the adsorption performance of multiwalled carbon nanotubes oxidized by varying degrees for removal of low levels of copper, nickel and chromium(VI) from aqueous solutions. *Water* **2020**, *12*, 723, https://doi.org/10.3390/w12030723.
33. Zarghami Dehaghani, M.; Yousefi, F.; Sajadi, S.M.; Tajammal Munir, M.; Abida, O.; Habibzadeh, S.; Mashhadzadeh, A.; Rabiee, N. Mostafavi, E.; Saeb, M.R. Theoretical encapsulation of fluorouracil (5-fu) anti-cancer chemotherapy drug into carbon nanotubes (cnt) and boron nitride nanotubes (bnnt). *Molecules* **2021**, *26*, 4920, https://doi.org/10.3390/molecules26164920.
34. Monajjemi, M. Liquid-phase exfoliation (LPE) of graphite towards graphene: An ab initio study. *Journal of Molecular Liquids* **2017**, *230*, 461–472, https://doi.org/10.1016/j.molliq.2017.01.044.
35. Jha, R.; Singh, A.; Sharma, P.K.; Fuloria, N.K. Smart carbon nanotubes for drug delivery system: A comprehensive study. *J. Drug Deliv. Sci. Technol.* **2020**, *58*, 101811, https://doi.org/10.1016/j.jddst.2020.101811.
36. Wei, Y.; Luo, J.; Huang, Y.; Chao, Y.; Wu, P.; Wang, L.; Dai, L.; Zhang, M.; Li, H.; Zhu, W. Binary molten salts mediated defect engineering on hexagonal boron nitride catalyst with long-term stability for aerobic oxidative desulfurization. *Appl. Surf. Sci.* **2021**, *558*, 149724, https://doi.org/10.1016/j.apsusc.2021.149724.
37. Wu, P.; Lu, L.; He, J.; Chen, L.; Chao, Y.; He, M.; Zhu, F.; Chu, X.; Li, H.; Zhu, W. Hexagonal boron nitride: A metal-free catalyst for deep oxidative desulfurization of fuel oils. *Green Energy Environ.* **2020**, *5*, 166–172, https://doi.org/10.1016/j.gee.2020.03.004.
38. Bakhshi, K.; Mollaamin, F.; Monajjemi, M. Exchange and correlation effect of hydrogen chemisorption on nano V(100) surface: A DFT study by generalized gradient approximation (GGA). *J.Comput.Theor.Nanosci*, **2011**, *8*,763-768, https://doi.org/10.1166/jctn.2011.1750.
39. Pham, D.T.; Tiyaboonchai, W. Fibroin nanoparticles: A promising drug delivery system. *Drug Deliv.* **2020**, *27*, 431–448, https://doi.org/10.1080/10717544.2020.1736208.
40. Monajjemi, M.; Baheri, H.; Mollaamin, F. A percolation model for carbon nanotube-polymer composites using the Mandelbrot-Given. *Journal of Structural Chemistry* **2011**, *52*, 54-59, https://doi.org/10.1134/S0022476611010070.

41. Reda, F.M.; El-Saadony, M.T.; Elnesr, S.S.; Alagawany, M.; Tufarelli, V. Effect of dietary supplementation of biological curcumin nanoparticles on growth and carcass traits, antioxidant status, immunity and caecal microbiota of Japanese quails. *Animals* **2020**, *10*, 754. https://doi.org/10.3390/ani10050754.
42. Legesse, M.; Rashkeev, S.N.; Saidaoui, H.; el Mellouhi, F.; Ahzi, S.; Alharbi, F.H. Band gap tuning in aluminum doped two-dimensional hexagonal boron nitride. *Mater. Chem. Phys.* **2020**, *250*, 123176, https://doi.org/10.1016/j.matchemphys.2020.123176.
43. Jacob, S.; Nair, A.B.; Shah, J. Emerging role of nanosuspensions in drug delivery systems. *Biomater. Res.* **2020**, *24*, 3, https://doi.org/10.1186/s40824-020-0184-8.
44. Chen, S.; Li, Q.; McClements, D.J.; Han, Y.; Dai, L.; Mao, L.; Gao, Y. Co-delivery of curcumin and piperine in zein-carrageenan core-shell nanoparticles: Formation, structure, stability and in vitro gastrointestinal digestion. *Food Hydrocoll.* **2020**, *99*, 105334, https://doi.org/10.1016/j.foodhyd.2019.105334.
45. Monajjemi, M.; Mohammadian, N.T. S-NICS: An aromaticity criterion for nano molecules. *Journal of Computational and Theoretical Nanoscience* **2015**, *12*, 4895-4914, https://doi.org/10.1166/jctn.2015.4458.
46. Wasfi, A.; Awwad, F.; Ayesh, A.I. DNA sequencing via Z-shaped graphene nano ribbon field effect transistor decorated with nanoparticles using first-principle transport simulations. *New J. Phys.* **2020**, *22*, 063004, https://doi.org/10.1088/1367-2630/ab87ef.
47. Li, H.; Ran, H.; Yujun, L.; Lv, N.; Yin, J.; Zhang, J.; Wang, C.; Jiang, W.; Zhu, W.; Li, H.; et al. Comparative Study of Halogen-Doped (X=Cl, Br, I) Hexagonal Boron Nitride: A Promising Strategy to Enhance the Capacity of Adsorptive Desulfurization. *J. Environ. Chem. Eng.* **2021**, *9*, 105886, https://doi.org/10.1016/j.jece.2021.105886.
48. Monajjemi, M.; Boggs, J.E. A New Generation of BnNn Rings as a Supplement to Boron Nitride Tubes and Cages. *J. Phys. Chem. A* **2013**, *117*, 1670-1684, http://dx.doi.org/10.1021/jp312073q.
49. Li, Y.; Lv, N.; Wang, C.; Zhang, J.; Fu, W.; Yin, J.; Li, H.; Zhu, W.; Li, H. Theoretical prediction of F-doped hexagonal boron nitride: A promising strategy to enhance the capacity of adsorptive desulfurization. *J. Mol. Graph. Model.* **2020**, *101*, 107715, https://doi.org/10.1016/j.jmgm.2020.107715.
50. Zhang, J.; Sun, R.; Ruan, D.; Zhang, M.; Li, Y.; Zhang, K.; Cheng, F.; Wang, Z.; Wang, Z.-M. Point defects in two-dimensional hexagonal boron nitride: A perspective. J. Appl. Phys. 2020, 128, 100902, https://doi.org/10.1063/5.0021093.
51. Weng, Q.; Zeng, L.; Chen, Z.; Han, Y.; Jiang, K.; Bando, Y.; Golberg, D. Hydrogen storage in carbon and oxygen co-doped porous boron nitrides. *Adv. Funct. Mater.* **2021**, *31*, 2007381, https://doi.org/10.1002/adfm.202007381.
52. Monajjemi, M. Quantum investigation of non-bonded interaction between the B15N15 ring and BH2NBH2 (radical, cation, and anion) systems: a nano molecularmotor. *Struct Chem* **2012,** *23*, 551–580, http://dx.doi.org/10.1007/s11224-011-9895-8.
53. Chao, Y.; Liu, M.; Pang, J.; Wu, P.; Jin, Y.; Li, X.; Luo, J.; Xiong, J.; Li, H.; Zhu, W. Gas-assisted exfoliation of boron nitride nanosheets enhancing adsorption performance. Ceram. Int. 2019, 45, 18838–18843, https://doi.org/10.1016/j.ceramint.2019.06.117.
54. Jia, J.; Wang, Y.; Feng, Y.; Hu, G.; Lin, J.; Huang, Y.; Zhang, Y.; Liu, Z.; Tang, C.; Yu, C. Hierarchically porous boron nitride/HKUST-1 hybrid materials: Synthesis, CO2 adsorption capacity, and CO2/N2 and CO2/CH4 selectivity. *Ind. Eng. Chem. Res.* **2021**, *60*, 2463–2471, https://doi.org/10.1021/acs.iecr.0c05701.
55. Song, Q.; Liang, J.; Fang, Y.; Guo, Z.; Du, Z.; Zhang, L.; Liu, Z.; Huang, Y.; Lin, J.; Tang, C. Nickel (II) modified porous boron nitride: An effective adsorbent for tetracycline removal from aqueous solution. *Chem. Eng. J.* **2020**, *394*, 124985, https://doi.org/10.1016/j.cej.2020.124985.
56. Monajjemi, M. Non bonded interaction between BnNn (stator) and BN B (rotor) systems: A quantum rotation in IR region. *Chemical Physics* **2013**, *425*, 29-45, https://doi.org/10.1016/j.chemphys.2013.07.014.
57. Chao, Y.; Zhang, J.; Li, H.; Wu, P.; Li, X.; Chang, H.; He, J.; Wu, H.; Li, H.; Zhu, W. Synthesis of boron nitride nanosheets with N-defects for efficient tetracycline antibiotics adsorptive removal. *Chem. Eng. J.* **2020**, *387*, 124138, https://doi.org/10.1016/j.cej.2020.124138.
58. Monajjemi, M. Metal-doped graphene layers composed with boron nitride–graphene as an insulator: a nanocapacitor. *Journal of Molecular Modeling* **2014**, *20*, 2507, https://doi.org/10.1007/s00894-014-2507-y.
59. Chao, Y.; Tang, B.; Luo, J.; Wu, P.; Tao, D.; Chang, H.; Chu, X.; Huang, Y.; Li, H.; Zhu, W. Hierarchical porous boron nitride with boron vacancies for improved adsorption performance to antibiotics. *J. Colloid Interf. Sci.* **2021**, *584*, 154–163, https://doi.org/10.1016/j.jcis.2020.09.075.
60. Becke, A.D. Density-functional thermochemistry. III. The role of exact exchange. *J Chem Phys* **1993**, 98, 5648–5652, https://doi.org/10.1063/1.464913

61. Lee, C.; Yang, W.; Parr, R.G. Development of the Colle–Salvetti correlation-energy formula into a functional of the electron density. *Phys Rev B* **1988**, *37*, 785–789, https://doi.org/10.1103/physrevb.37.785.
62. Kim, K.; Jordan, K.D. Comparison of Density Functional and MP2 Calculations on the Water Monomer and Dimer. *J. Phys. Chem.* **1994**, *98*, 10089–10094, https://doi.org/10.1021/j100091a024.
63. Stephens, P.J.; Devlin, F. J. Chabalowski,C. F. Frisch M. J. Ab Initio Calculation of Vibrational Absorption and Circular Dichroism Spectra Using Density Functional Force Fields. *J. Phys. Chem.* **1994**, *98*, 11623–11627, https://doi.org/10.1021/j100096a001.
64. Cramer, C.J. *Essentials of Computational Chemistry: Theories and Models*, 2nd Edition *Wiley*. **2004**.
65. Vosko, S.H.; Wilk, L.; Nusair, M. Accurate spin-dependent electron liquid correlation energies for local spin density calculations: a critical analysis. *Can. J. Phys.* **1980**, *58* ,1200–1211, https://doi.org/10.1139/p80-159.
66. Monajjemi, M.; Heshmat, M.; Haeri, H.H.; Kaveh, F. Theoretical study of vitamin properties from combined QM-MM methods: Comparison of chemical shifts and energy. *Russian Journal of Physical Chemistry* **2006**, *80*, 1061, https://doi.org/10.1134/S0036024406070119.
67. Zadeh, Mahsa Ali Akbari; Lari, Hadi; Kharghanian, Leyla; Balali, Ebrahim; Khadivi, Ramona; Yahyaei, Hooriye; Mollaamin, Fatemeh; Monajjemi, Majid, Density functional theory study and anti-cancer properties of shyshaq plant: In view point of nano biotechnology, *Journal of Computational and Theoretical Nanoscience* **2015**, *12*, 4358-4367, https://doi.org/10.1166/jctn.2015.4366.
68. Monajjemi, M.; Baie, M.T.; Mollaamin, F. Interaction between threonine and cadmium cation in [Cd(Thr)] (n = 1-3) complexes: Density functional calculations , *Russian Chemical Bulletin* , **2010**, *59*, 886-889, https://doi.org/10.1007/s11172-010-0181-5.
69. Cramer, C.J.; Truhlar,D.G. PM3-SM3: A general parameterization for including aqueous solvation effects in the PM3 molecular orbital model. *J.Comp.Chem.* **1992**, *13*, 1089-1097. https://doi.org/10.1002/jcc.540130907.
70. Sarasia, E.M.; Afsharnezhad, S.; Honarparvar, B.; Mollaamin, F.; Monajjemi, M. Estrogenic active stilbene derivatives as anti-cancer agents: A DFT and QSAR study. *Phys. Chem. Liq*. **2011**, *49*, 561-571, https://doi.org/10.1080/00319101003698992.
71. Chambers,C.C.; Hawkins,G.D.; Cramer,C.J.; Truhlar,D.G. Model for Aqueous Solvation Based on Class IV Atomic Charges and First Solvation Shell Effects. *J.Phys.Chem.***1996**, *100*, 16385-16398, https://doi.org/10.1021/jp9610776
72. Khaleghian, M.; Zahmatkesh, M.; Mollaamin, F.; Monajjemi, M. Investigation of Solvent Effects on Armchair Single-Walled Carbon Nanotubes: A QM/MD Study. *Fuller. Nanotub. Carbon Nanostructures.* **2011,** *19*, 251-261, https://doi.org/10.1080/15363831003721757.
73. Onsager,L.J. Electric Moments of Molecules in Liquids. *J Am. Chem. Soc.* **1936**, *58*, 1486-1493, https://doi.org/10.1021/ja01299a050
74. Ghalandari, B.; Monajjemi, M.; Mollaamin, F. Theoretical Investigation of Carbon Nanotube Binding to DNA in View of Drug Delivery. *J.Comput.Theor.Nanosci* **2011**, *8*, 1212-1219, https://doi.org/10.1166/jctn.2011.1801.
75. Tomasi, J. Cavity and reaction field: "robust" concepts. Perspective on "Electric moments of molecules in liquids". *Theor.Chem.Acc.* **2000**, *103*,196-199, https://doi.org/10.1007/s002149900044.
76. Frisch, M. J.; Trucks, G. W.; Schlegel, H. B.; Scuseria, G. E.; Robb, M. A.; Cheeseman, J. R.; Scalmani, G.; Barone, V.; Petersson, G. A.; Nakatsuji, H.; Li, X.; Caricato, M.; Marenich, A. V.; Bloino, J.; Janesko, B. G.; Gomperts, R.; Mennucci, B.; Hratchian, H. P.; Ortiz, J. V.; Izmaylov, A. F.; Sonnenberg, J. L.; Williams-Young, D.; Ding, F.; Lipparini, F.; Egidi, F.; Goings, J.; Peng, B.; Petrone, A.; Henderson, T.; Ranasinghe, D.; Zakrzewski, V. G.; Gao, J.; Rega, N.; Zheng, G.; Liang, W.; Hada, M.; Ehara, M.; Toyota, K.; Fukuda, R.; Hasegawa, J.; Ishida, M.; Nakajima, T.; Honda, Y.; Kitao, O.; Nakai, H.; Vreven, T.; Throssell, K.; Montgomery, J. A., Jr.; Peralta, J. E.; Ogliaro, F.; Bearpark, M. J.; Heyd, J. J.; Brothers, E. N.; Kudin, K. N.; Staroverov, V. N.; Keith, T. A.; Kobayashi, R.; Normand, J.; Raghavachari, K.; Rendell, A. P.; Burant, J. C.; Iyengar, S. S.; Tomasi, J.; Cossi, M.; Millam, J. M.; Klene, M.; Adamo, C.; Cammi, R.; Ochterski, J. W.; Martin, R. L.; Morokuma, K.; Farkas, O.; Foresman, J. B.; Fox, D. J. *Gaussian 16, Revision C.01*, Gaussian, Inc., Wallingford CT, **2016**, https://www.scirp.org/(S(lz5mqp453ed%20snp55rrgjct55))/reference/referencespapers.aspx?referenceid=2418053.
77. Monajjemi, M. Cell membrane causes the lipid bilayers to behave as variable capacitors: A resonance with self-induction of helical proteins. *Biophysical Chemistry* **2015**, *207*, 114-127, https://doi.org/10.1016/j.bpc.2015.10.003.

78. Tahan, A.; Mollaamin, F.; Monajjemi, M. Thermochemistry and NBO analysis of peptide bond: Investigation of basis sets and binding energy. *Russian Journal of Physical Chemistry A* **2009**, *83*, 587-597, https://doi.org/10.1134/S003602440904013X.
79. Monajjemi, M.; Honaparvar, B.; Khalili Hadad, B.; Ilkhani, A.; Mollaamin, F. Thermo-Chemical Investigation and NBO Analysis of Some anxileotic as Nano- Drugs. *African journal of pharmacy and pharmacology* **2010**, *4*, 521-529, https://www.researchgate.net/publication/304742272.
80. Khalili Hadad, B.; Mollaamin, F.; Monajjemi, M. Biophysical chemistry of macrocycles for drug delivery: A theoretical study. *Russian Chemical Bulletin* **2022**,60, 238-241, https://doi.org/10.1007/s11172-011-0039-5.
81. Mollaamin, Fatemeh; Ilkhani, Alireza; Sakhaei, Neda; Bonsakhteh, Behnaz; Faridchehr, Afsaneh; Tohidi, Sogand; Monajjemi, Majid, Thermodynamic and solvent effect on dynamic structures of nano bilayer-cell membrane: Hydrogen bonding study. *Journal of Computational and Theoretical Nanoscience* **2015**, *12*, 3148-3154, https://doi.org/10.1166/jctn.2015.4092.
82. Mollaamin,F.; Shahriari.; Monajjemi,M.; Khalaj, Z. Nanocluster of Aluminum Lattice via Organic Inhibitors Coating: A Study of Freundlich Adsorption. Journal of Cluster Science 2022, 1-16. https://doi.org/10.1007/s10876-022-02335-1.
83. Fry, R.A.; Kwon, K.D.; Komarneni,S.; Kubicki, J.D.; Mueller,K.T. Solid-State NMR and Computational Chemistry Study of Mononucleotides Adsorbed to Alumina. *Langmuir* **2006**, *22*, 9281-9286, https://doi.org/10.1021/la061561s.
84. Chen. K. A Practical Review of NMR Lineshapes for Spin-1/2 and Quadrupolar Nuclei in Disordered Materials. *Int. J. Mol. Sci.* **2020**, *21*, 5666, https://doi.org/10.3390/ijms21165666.
85. Smith, J.A.S. Nuclear Quadrupole Resonance Spectroscopy. *Journal of Chemical Education.* **1971**, *48*, 39–41, https://doi.org/10.1021/ed048p39.
86. Peng,J.; Xiao,Y.; Clarkson,D.A.; Greenbaum,S.G.; Zawodzinski,T.A.; Chen.X.C. A Nuclear Magnetic Resonance Study of Cation and Anion Dynamics in Polymer–Ceramic Composite Solid Electrolytes. *ACS Applied Polymer Materials* **2020**, *2*, 1180-1189, https://doi.org/10.1021/acsapm.9b01068.
87. Kravchenko, E.A.; Orlov, V. G.; Sergeev. G. S. Magnetic Properties of Sb2S3 and Bi2S3 as Evidenced by 121,123Sb and 209Bi NQR Spectra. *Journal of Experimental and Theoretical Physics* **2020**, *131*, 761-767, https://doi.org/10.1134/S1063776120100064.
88. Aihara, J.; Reduced HOMO−LUMO Gap as an Index of Kinetic Stability for Polycyclic Aromatic Hydrocarbons. *J. Phys. Chem. A* **1999**, *103*, 37, 7487–7495, https://doi.org/10.1021/jp990092i.
89. Kohn, W.; Becke, A.D.; Parr, R.G. Density Functional Theory of Electronic Structure. *J. Phys. Chem*. **1996**, *100*, 12974–12980, https://doi.org/10.1021/jp960669l.
90. Parr, R.G.; Pearson, R.G. Absolute Hardness: Companion Parameter to Absolute Electronegativity. *J. Am. Chem. Soc.* **1983**, *105*, 7512-7516, http://dx.doi.org/10.1021/ja00364a005.
91. Politzer, P.; Abu-Awwad, F. A comparative analysis of Hartree-Fock and Kohn-Sham orbital energies. *Theor. Chem. Acc.* **1998**, *99*, 83–87, https://doi.org/10.1007/s002140050307.